Defects, diffusion and dopants in the ceramic mineral “Lime- Feldspar”

Sivanujan Suthaharan, Poobalasuntharam Iyngaran, Navaratnarajah Kuganathan, and Alexander Chroneos

Original citation & hyperlink:
Suthaharan, S., Iyngaran, P., Kuganathan, N. and Chroneos, A., 2021. Defects, diffusion and dopants in the ceramic mineral “Lime-Feldspar”. *Journal of Asian Ceramic Societies*, Vol 9, Issue 2, pp.570-577
https://dx.doi.org/10.1080/21870764.2021.1903686

DOI 10.1080/21870764.2021.1903686
ISSN 2187-0764

Publisher: Taylor and Francis

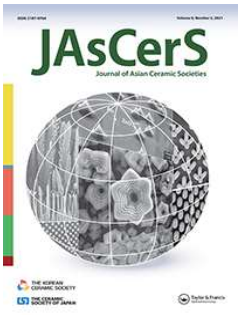

Journal of Asian Ceramic Societies

ISSN: (Print) (Online) Journal homepage: https://www.tandfonline.com/loi/tace20

Defects, diffusion and dopants in the ceramic mineral “Lime- Feldspar”

Sivanujan Suthaharan, Poobalasuntharam Iyngaran, Navaratnarajah Kuganathan & Alexander Chroneos

To cite this article: Sivanujan Suthaharan, Poobalasuntharam Iyngaran, Navaratnarajah Kuganathan & Alexander Chroneos (2021) Defects, diffusion and dopants in the ceramic mineral “Lime- Feldspar”, Journal of Asian Ceramic Societies, 9:2, 570-577, DOI: 10.1080/21870764.2021.1903686

To link to this article: https://doi.org/10.1080/21870764.2021.1903686

Published online: 11 Apr 2021.

JOURNAL OF ASIAN CERAMIC SOCIETIES
2021, VOL. 9, NO. 2, 570–577
https://doi.org/10.1080/21870764.2021.1903686

THE CERAMIC SOCIETY OF JAPAN · THE KOREAN CERAMIC SOCIETY · Taylor & Francis
Taylor & Francis Group

FULL LENGTH ARTICLE

Defects, diffusion and dopants in the ceramic mineral "Lime- Feldspar"

Sivanujan Suthaharan[a], Poobalasuntharam Iyngaran[a], Navaratnarajah Kuganathan[b,c] and Alexander Chroneos[c]

[a]Department of Chemistry, University of Jaffna, Thirunelvely, Jaffna, Srilanka; [b]Department of Materials, Imperial College London, London, UK; [c]Faculty of Engineering, Environment and Computing, Coventry University, Coventry, UK

ABSTRACT

Calcium aluminosilicate, $CaAl_2Si_2O_8$, is a promising ceramic material that has found applications in several areas, such as glass production and petrology. Atomistic scale simulation techniques are used to study the intrinsic defects, Ca-ion migration paths and doping behavior in $CaAl_2Si_2O_8$. The most favorable defect is the Al–Si anti-site in agreement with the experimental observation. The O-Frenkel is the second most favorable defect. The Ca-Frenkel is higher in energy only by 0.62 eV than the O-Frenkel. Long-range Ca-ion migration is observed in the *ac* plane with the activation energy of 2.84 eV suggesting that Ca-ion diffusion in this material is slow. The prominent isovalent dopant on the Ca site is the Sr, which was experimentally substituted on the Ca site to prevent phase transformation. The formation of Ca interstitials and oxygen vacancies is favored by Fe^{3+} doping on the Si site. The favorable tetravalent dopant on the Si site and the Al site to form Ca vacancies is the Ge.

ARTICLE HISTORY
Received 7 September 2020
Accepted 11 March 2021

KEYWORDS
$CaAl_2Si_2O_8$; defects; ca-ion diffusion; dopants; atomistic simulation

1. Introduction

Anorthite ($CaAl_2Si_2O_8$), also termed lime-feldspar, is a naturally occurring rock-forming mineral found in many countries including Italy, Japan, USA, India and Srilanka [1–3]. It is a potential ceramic material in the industrial preparation of heat exchangers, feldspar glasses, electronic substrates and materials required for biomedicine [4–7]. As its crystalline phase, it can improve the translucent property of bone china, there is an increasing attention to prepare anorthite-based porcelain to make tableware with high heat stability [8]. Furthermore, calcium-bearing minerals are of interest in the development of electrode materials for rechargeable Ca-ion batteries [9]. Though $CaAl_2Si_2O_8$ was not studied for this purpose yet, theoretical investigation on other Ca-based minerals is available [10–12].

There have been extensive research efforts to study its physical and mechanical properties during the past few decades in order to develop this ceramic material for industrial applications [13–15]. Anorthite porcelain synthesized by Pal *et al.* [13] exhibited low thermal expansion coefficient inferring its usage in cooking wares. Le Parc *et al.* [16] used Raman spectroscopy and neutron scattering experiment to compare the rigidity and disorder behavior of $CaAl_2Si_2O_8$ glass structure with that of the anorthite crystal structure. At high temperatures and pressures, this material undergoes partial Al/Si disorder leading to phase transition [17,18]. The addition of Fe_2O_3 not only improves its crystalline behavior but also provides color to its glasseous form [18,19]. McGuinn *et al.* [20] have shown that doping of Sr^{2+} or Ba^{2+} on the Ca site in $CaAl_2SiO_8$ can prevent phase transition and increase its symmetry [21,22]. Though there are many experimental studies available on this material, only a few theoretical works have been reported. Molecular dynamics simulation has been carried by Karki *et al.* [21] to look at the diffusion and viscosity of molten $CaAl_2Si_2O_8$ at different temperatures and pressures. In a density functional theory (DFT) study by Zhang *et al.* [23], the surface structure of anorthite was considered for the adsorption of CO_2 molecules and the influence of water on its adsorption predicted.

The fundamental understanding of intrinsic and extrinsic defects in $CaAl_2Si_2O_8$ can be useful to optimize its performance in ceramic and battery industries. Atomistic simulations based on the classical pair potentials can provide valuable information about defect processes including cation disorder, self-diffusion and promising dopants in $CaAl_2Si_2O_8$. This simulation technique has been successfully used to model crystalline materials over the last two decades and has provided experiments with unique insight and prediction [24–28]. To the best of our knowledge, there is no simulation study on the defects, diffusion and dopant reported for $CaAl_2Si_2O_8$ in the literature. In this work, we report the results of intrinsic defect processes, Ca-diffusion pathways together with activation energies and solution of MO (M = Co, Mn, Ni, Mg, Zn, Sr and Ba), M_2O_3 (M = Ga, Fe, In, Sc, Y, Gd and La) and MO_2 (M = Ge, Ti, Sn, Zr and Ce) in $CaAl_2Si_2O8$

CONTACT Navaratnarajah Kuganathan n.kuganathan@imperial.ac.uk Department of Materials, Imperial College London, SW7 2AZ, London UK

Table 1. Buckingham potential parameters [30,31]used in the classical simulations of $CaAl_2Si_2O_8$. Two-body [$\Phi_{ij}(r_{ij}) = A_{ij}\exp(-r_{ij}/\rho_{ij}) - C_{ij}/r_{ij}^6$] where A, ρ and C are parameters that were selected carefully to reproduce the experimental data. The values of Y and K represent the shell charges and spring constants. A very large spring constant means there is no shell charge and the atom is treated as the core.

Interaction	A/eV	ρ/Å	C/eV·Å^6	Y/e	K/eV·Å^{-2}
Ca^{2+}–O^{2-}	1090.40	0.34370	0.00	3.135	110.20
Al^{3+}–O^{2-}	1114.90	0.31180	0.00	3.000	99,999.00
Si^{4+} O^{2-}	1283.91	0.32052	10.66	4.000	99,999.00
O^{2-}–O^{2-}	22,764.00	0.1490	27.89	2.040	27.29

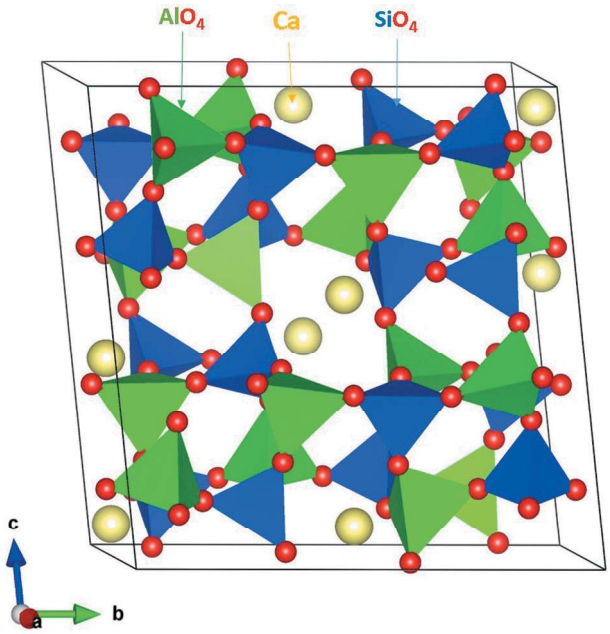

Figure 1. Crystal structure of triclinic CaAl2Si2O8 (space group $P\bar{1}$).

2. Computational methods

All calculations were performed using a classical pair-wise potential simulation code GULP (General Utility Lattice Program) [29]. Interactions between ions were modeled using long-range (Coulombic) and short-range (Pauli repulsion and van der Waals attraction). The Buckingham potentials were used to model short-range repulsive forces (see Table 1) [30,31]. Full geometry relaxations were carried out using the Broyden-Fletcher-Goldfarb-Shanno (BFGS) algorithm [32]. Forces on all ions in the relaxed configurations were smaller than 0.001 eV/Å. The Mott–Littleton method [33] was used to model point defects. The methodology to calculate migration ion pathway together with activation energy has been well explained in the previous simulation work [34]. The current methodology treats ions as a spherical shape with full charge at the dilute limit. Therefore, it is anticipated that calculated defect energies will be overestimated. However, the trend in relative energies will be consistent [35].

3. Results and discussion

3.1. Crystal structure of $CaAl_2Si_2O_8$

The crystal structure of $CaAl_2Si_2O_8$ (lattice parameters: a = 8.186 Å, b = 12.876 Å, c = 14.182 Å, α = 93.3°, β = 115.79° and γ = 91.12°) belongs to triclinic phase with $P\bar{1}$ symmetry as reported by Bruno *et al.* [36]. Both

Table 2. Calculated and experimental lattice parameters of $CaAl_2Si_2O_8$.

Parameter	Calculated	Experiment [36]	|Δ|(%)
a (Å)	8.36	8.19	2.09
b (Å)	12.93	12.88	0.39
c (Å)	14.04	14.18	1.02
α (°)	92.26	93.30	1.11
β (°)	114.84	115.79	0.82
γ (°)	90.78	91.12	0.37

Al and Si form tetrahedral units and they are interlinked by sharing their corners (see Figure 1).

Both ionic positions and lattice constants were relaxed (full geometry optimization) to obtain equilibrium lattice constants and compare with corresponding experimental values in order to validate the choice of potential parameters in this study. Initial and final lattice parameters are reported in Table 2. There is a good agreement between the calculated and experimental lattice parameters indicating the efficacy of the potentials.

3.2. Intrinsic defect processes

Defects play a significant role in mechanical and diffusion properties of a material. A series of isolated point defects (vacancies and interstitials) were calculated and then they were combined to calculate Frenkel and Schottky defect formation energies. The anti-site defects were also considered in the form of isolated and cluster. Impurity defects (e.g., Al'_{Si} and $Si^{\bullet}_{Al}$) *were considered separately and their defect energies were combined to calculate the anti-site (isolated) reaction energy. In the case of cluster form, both defects were considered simultaneously. The difference between the defect energies {E (cluster) –E (isolated)} is defined as binding energy. Defect reaction energies as written using Kröger-Vink notation [37] are shown in equations 1–14.*

$$CaFrenkel: Ca^{X}_{Ca} \rightarrow V''_{Ca} + Ca^{\bullet\bullet}_{i} \quad (1)$$

$$AlFrenkel: Al^{X}_{Al} \rightarrow V'''_{Al} + Al^{\bullet\bullet\bullet}_{i} \quad (2)$$

$$Si\,Frenkel: V^{X}_{Si} \rightarrow V''''_{Si} + Si^{\bullet\bullet\bullet\bullet}_{i} \quad (3)$$

$$O\,Frenkel: O^{X}_{O} \rightarrow V^{\bullet\bullet}_{O} + O''_{i} \quad (4)$$

Table 3. Reaction energies calculated for Schottky, Frenkel and anti-site defects.

Defect process	equation	Reaction energy (eV)	Reaction energy (eV)/ defect
Ca Frenkel	1	4.00	3.63
Al Frenkel	2	12.72	6.36
Si Frenkel	3	22.30	11.15
O Frenkel	4	6.02	3.01
Schottky	5	96.59	7.43
CaO Schottky	6	9.06	4.53
Al_2O_3 Schottky	7	8.80	4.40
SiO_2 Schottky	8	18.10	9.05
Ca/Al anti-site (isolated)	9	8.58	4.29
Ca/Al anti-site (cluster)	10	6.56	3.28
Ca/Si anti-site (isolated)	11	14.24	7.12
Ca/Si anti-site (cluster)	12	8.48	4.24
Al/Si anti-site (isolated)	13	1.72	0.86
Al/Si anti-site (cluster)	14	0.78	0.39

$$Schottky: Ca^{X}_{Ca} + 2Al^{X}_{Al} + 2Si^{X}_{Si} + 8O^{X}_{O} \rightarrow V''_{Ca} + 2V'''_{Al} + 2V''''_{Si} + 8V^{\bullet\bullet}_{O} + CaAl_2Si_2O_8 \quad (5)$$

$$CaOSchottky: Ca^{X}_{Ca} + O^{X}_{O} \rightarrow V''_{Ca} + V^{\bullet\bullet}_{O} + CaO \quad (6)$$

$$Al_2O_3Schottky: 2Al^{X}_{Al} + 3O^{X}_{O} \rightarrow 2V'''_{Al} + 3V^{\bullet\bullet}_{O} + Al_2O_3 \quad (7)$$

$$SiO_2Schottky: Si^{X}_{Si} + 2O^{X}_{O} \rightarrow V''''_{Si} + 2V^{\bullet\bullet}_{O} + SiO_2 \quad (8)$$

$$Ca/Alantisite(isolated): Ca^{X}_{Ca} + Al^{X}_{Al} \rightarrow Ca'_{Al} + Al^{\bullet}_{Si} \quad (9)$$

$$Ca/Alantisite(cluster): Ca^{X}_{Ca} + Al^{X}_{Al} \rightarrow \{Ca'_{Al} : Al^{\bullet}_{Si}\}^{X} \quad (10)$$

$$Ca/Siantisite(isolated): Ca^{X}_{Ca} + Si^{X}_{Si} \rightarrow Ca''_{Si} + Si^{\bullet\bullet}_{Ca} \quad (11)$$

$$Ca/Siantisite(cluster): Ca^{X}_{Ca} + Si^{X}_{Si} \rightarrow \{Ca''_{Si} : Si^{\bullet\bullet}_{Ca}\}^{X} \quad (12)$$

$$Al/Siantisite(isolated): Al^{X}_{Al} + Si^{X}_{Si} \rightarrow Al'_{Si} + Si^{\bullet}_{Al} \quad (13)$$

$$Al/Siantisite(cluster): Al^{X}_{Al} + Si^{X}_{Si} \rightarrow \{Al'_{Si} : Si^{\bullet}_{Al}\}^{X} \quad (14)$$

Table 3 reports the reaction energies calculated for different defect processes. The Al–Si anti-site cluster is the most dominant defect inferring the presence of cation intermixing [Al on the Si site (Al'_{Si}) and Si on the Al site ($Si^{\bullet}_{Al}$)] in $CaAl_2Si_2O_8$. This result is in agreement with the experimental observation of Al/Si disorder at high temperature [17,18]. Exoergic binding energy of –0.47 eV shows that isolated defects (Al'_{Si} and $Si^{\bullet}_{Al}$) are not stable and they aggregate to form clusters ($Al'_{Si} : Si^{\bullet}_{Al})^{X}$ without an energy penalty. In many oxide materials, the anti-site defect has been identified experimentally and theoretically [38–41]. The O Frenkel is identified as the second most favorable defect energy process. However, this process would require moderate temperature. Other Frenkel and Schottky defect processes exhibit high endothermic energies implying that they are highly unlikely to occur at normal temperatures. The formation of CaO in this material was considered via CaO Schottky-like reaction (equation 6). The formation energy for this process is 4.53 eV per defect suggesting that formation of V''_{Ca} and $V^{\bullet\bullet}_{O}$ in this material is only possible at high temperatures.

3.3. Calcium ion diffusion

The performance of a material is partly dependent on its diffusion properties. The diffusion of Ca-ions in this material can be of interest in the application of Ca-ion batteries. Materials exhibiting long-range Ca-ion diffusion with low activation energy are one of the essential

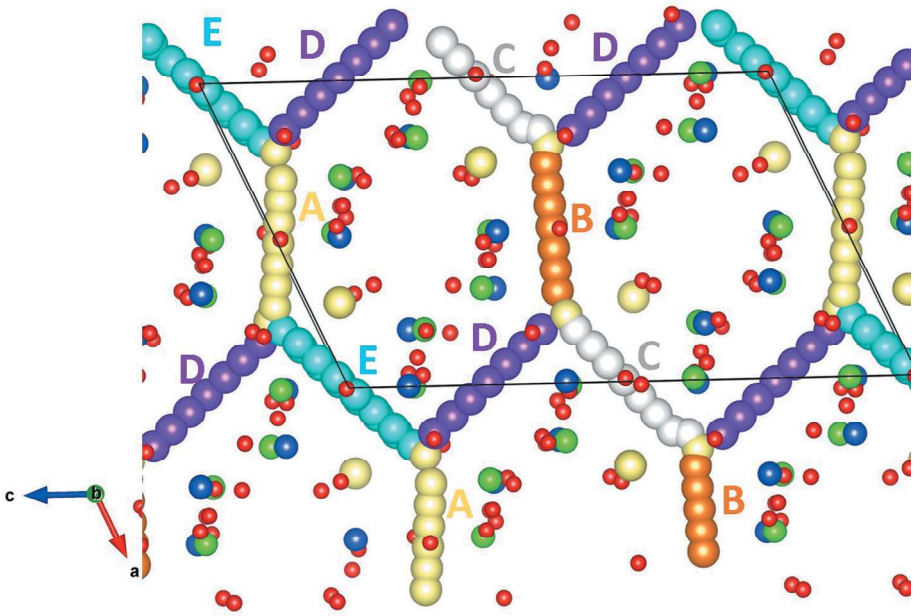

Figure 2. Possible long-range calcium vacancy migration paths considered in CaAl2Si2O8. Yellow, white, blue, orange and purple color atoms correspond to different Ca hopping trajectories.

Table 4. Calculated Ca-Ca separations and corresponding activation energies (see Figure 3).

Migration path	Ca-Ca separation (Å)	Activation energy (eV)
A	4.19	2.97
B	4.25	2.60
C	4.65	2.96
D	4.93	2.58
E	5.07	2.84

conditions for constructing a promising Ca-ion battery. However, it is expected that the Ca-ion diffusion in Ca-bearing oxide materials would be slow due to its ion size with a double positive charge. Previous quantum mechanical simulations [10,42] analyzed the suitability of minerals as electrode materials for Ca-ion batteries and high activation energies of migration confirmed the slow diffusivity ion of Ca-ions. Atomistic simulations based on the classical pair potentials can provide useful information on diffusion pathways and activation energies as this information is generally difficult from the experiment. The present methodology has been successfully applied to various ionic materials to calculate migration pathways together with activation energies [11,12,25,26]. For example, there is an excellent agreement between calculated and experimentally determined Li-ion diffusion pathway in $LiFePO_4$ [43,44].

Five different local Ca hops (see Figure 2) were identified for the vacancy-mediated Ca-ion migration. Local Ca hops with their separations and corresponding activation energies are reported in Table 4. Activation energies for individual Ca hops are greater than 2.50 eV suggesting that Ca-ion diffusion in this material is very limited. Figure 3 shows the energy profile diagrams calculated for local hops. Local hops were connected in different ways to construct long-range diffusion pathways (see Table 5). In all cases, the movement of Ca-ions is observed in the ac plane. The pathway with the lowest activation energy of 2.84 eV is noted for D↔E↔D↔B. Other pathways exhibit slightly higher activation energies only by ~0.13 eV than that calculated for the lowest energy pathway. We should add that we have considered a range of other paths with longer Ca-Ca hoping distances of >5.75 Å, but these were all found to have prohibitively high migration barriers (>4 eV).

3.4. Solution of dopants

The performance of a material is partially dominated by the substitutional dopants. A range of dopants were considered for screening and predicting promising dopants that can be verified experimentally. Appropriate charge-compensation defects and lattice energies were introduced to calculate solution energies. In the supplementary information, Buckingham potentials used for dopants are provided (see Table S1).

3.4.1. Divalent dopants

First, divalent dopants (M = Co, Mn, Ni, Mg, Zn, Sr and Ba) were considered on the Ca site. The following equation was used to calculate the solution energy.

$$MO + Ca_{Ca}^{X} \rightarrow M_{Ca}^{X} + CaO \qquad (15)$$

Exothermic solution energy is calculated for Sr^{2+} and Ba^{2+} suggesting that they are the most prominent dopants on the Ca site (see Table 6). Possible composition that can be available in nature or from experimental preparation is $Ca_{1-x}M_xAl_2Si_2O_8$ (M = Sr or Ba and $0.0 < x < 1.0$). Experimental preparation of $Ca_{1-x}Sr_xAl_2Si_2O_8$ has been considered to prevent the distortion of monoclinic and triclinic forms of $CaAl_2Si_2O_8$ [20]. Other

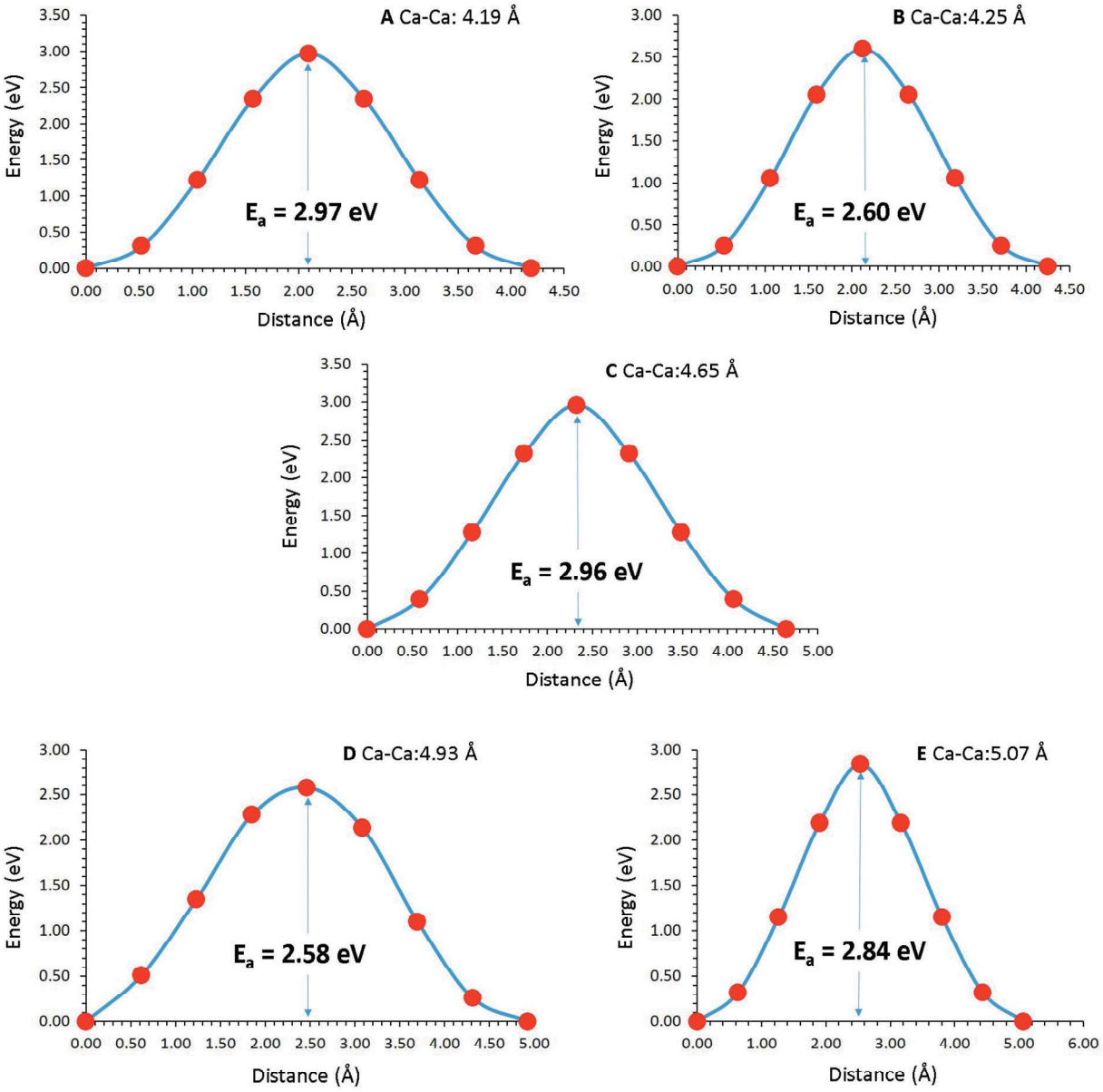

Figure 3. Five different energy profiles (as shown in Figure 2) of Ca vacancy hopping between two adjacent Ca sites.

Table 5. Possible long-range Ca ion diffusion paths and their corresponding activation energies (see Figure 2).

Long-range path	Activation energy (eV)
A E A D	2.97
A D B C	2.97
A D B D	2.97
A E B E	2.97
A D C B	2.97
B C B C	2.96
B C B D	2.96
D E D B	2.84

Table 6. Solution energy of MO (M = Co, Mn, Ni, Mg, Zn, Sr and Ba) with respect to the M^{2+} ionic radius (see equation 15).

M^{2+} ion	Ionic radius (Å)	Solution energy (eV/M^{2+} ion)
Co^{2+}	0.65	1.77
Mn^{2+}	0.67	1.52
Ni^{2+}	0.69	2.01
Mg^{2+}	0.72	1.87
Zn^{2+}	0.74	1.63
Sr^{2+}	1.18	0.64
Ba^{2+}	1.35	0.59

dopants exhibit endoergic solution energies. They are unlikely to be doped at normal temperatures. High preference of Sr^{2+} can be due to its ionic radius (1.18 Å) close to the ionic radius of Ca^{2+} (1.00 Å).

3.4.2. *Trivalent doping*

Next, a range of trivalent dopants (M = Ga, Fe, In, Sc, Y, Gd and La) were considered on the Al site. The following equation explains the defect process in which trivalent dopants are substituted on the Al site without introducing charge compensating defects.

$$M_2O_3 + 2Al_{Al}^{X} \rightarrow 2M_{Al}^{X} + Al_2O_3 \qquad (16)$$

Table 7 reports the solution energies calculated for this process. The most favorable dopant is the Fe^{3+} with the solution energy of 0.23 eV per dopant. This dopant is particularly important in the glass industry as the

Table 7. Solution energy of M_2O_3 (M = Ga, Fe, In, Sc, Y, Gd and La) with respect to the M^{3+} ionic radius (see equation 16).

M^{3+} ion	Ionic radius (Å)	Solution energy (eV/M^{3+} ion)
Ga^{3+}	0.47	1.24
Fe^{3+}	0.49	0.23
In^{3+}	0.62	1.03
Sc^{3+}	0.75	0.71
Y^{2+}	0.90	1.19
Gd^{3+}	0.94	1.59
La^{3+}	1.03	1.47

Table 8. Solution energy calculated for the introduction of Ca interstitials (see equation 17) and oxygen vacancies *via* M^{3+} doping on the Si site (see equation 18).

		Solution energy (eV/M^{3+} ion)	
M^{3+} ion	Ionic radius (Å)	Ca interstitials	Oxygen vacancies
Ga^{3+}	0.47	4.29	4.91
Fe^{3+}	0.49	3.27	3.89
In^{3+}	0.62	3.78	4.40
Sc^{3+}	0.75	4.09	4.72
Y^{2+}	0.90	4.29	4.93
Gd^{3+}	0.94	4.68	5.30
La^{3+}	1.03	4.57	5.19

Table 9. Solution energy of MO_2 (R = Ge, Ti, Sn, Zr and Ce) calculated by the substitutional doping of M^{4+} ion on the Si site with respect to the M^{4+} ionic radius (see equation 19).

M^{4+} ion	Ionic radius (Å)	Solution energy (eV/M^{4+} ion)
Ge^{4+}	0.32	0.37
Ti^{4+}	0.42	3.55
Sn^{4+}	0.55	1.89
Zr^{4+}	0.59	2.51
Ce^{4+}	0.87	3.44

presence of a small amount of Fe^{3+} in the feldspar glasses makes them colorful [18]. The Sc^{3+} is identified as the second most favorable dopant and its solution energy is 0.71 eV. High positive solution energies (>1 eV) are calculated for the other dopants suggest that this process is possible at high temperatures.

Thereafter, the Si site was considered for doping of trivalent dopants. In this case, negative charges are introduced in the lattice and they are compensated by positively charged Ca interstitials. This process will lead to the formation of additional Ca in the lattice. The formation of Ca interstitials can increase the capacity of $CaAl_2Si_2O_8$ and enhance the diffusion of Ca ion. The following equation was used to calculate the solution energy for this process.

$$M_2O_3 + 2Si_{Si}^{X} + CaO \rightarrow 2M'_{Si} + Ca_i^{\bullet\bullet} + 2SiO_2 \qquad (17)$$

Calculated solution enthalpies are shown in Table 8. The most favorable dopant is Fe^{3+} with the solution energy of 3.27 eV though its solution energy is endothermic. The possible composition would be $Ca_{1+x}AlFe_xSi_{1-x}O_8$ ($0.0 < x < 1.0$). The second most favorable dopant is In^{3+}. Other dopants exhibit high solution energies (>4 eV) meaning they are highly unlikely to take place at normal temperatures.

Table 10. Solution energy of MO_2 (R = Ge, Ti, Sn, Zr and Ce) calculated by the substitutional doping of M^{4+} ion on the Al site with respect to the M^{4+} ionic radius (see equation 20).

M^{4+} ion	Ionic radius (Å)	Solution energy (eV/M^{4+} ion)
Ge^{4+}	0.32	2.50
Ti^{4+}	0.42	5.80
Sn^{4+}	0.55	3.76
Zr^{4+}	0.59	4.28
Ce^{4+}	0.87	5.22

Table 11. Calculated activation energies for the local Ca hoping and the long-range diffusion pathways in the presence of favorable dopants. The numbers in bold show the lowest activation energy for the long-range Ca diffusion.

	Activation energy (eV)		
hops	Sr_{Ca}^{X}	Fe_{Al}^{X}	Ge_{Si}^{X}
A	2.90	2.93	2.89
B	2.62	2.64	2.58
C	2.88	2.92	2.89
D	2.50	2.53	2.55
E	2.80	2.79	2.82
Long range path	Sr_{Ca}^{X}	Fe_{Al}^{X}	Ge_{Si}^{X}
A E A D	2.90	2.93	2.89
A D B C	2.90	2.93	2.89
A D B D	2.90	2.93	2.89
A E B E	2.90	2.93	2.89
A D C B	2.90	2.93	2.89
B C B C	2.88	2.92	2.89
B C B D	2.88	2.92	2.89
D E D B	**2.80**	**2.89**	**2.82**

Trivalent dopants on the Si site can introduce oxygen vacancies as charge compensating defects as described by the following equation.

$$M_2O_3 + 2Si_{Si}^{X} + CaO \rightarrow 2M'_{Si} + V_O^{\bullet\bullet} + 2SiO_2 \qquad (18)$$

Calculations reveal that the Fe^{3+} is the most favorable dopant (see Table 8). The trend in solution energy is the same as calculated for Ca interstitial as charge compensating defect.

3.4.3. Tetravalent doping

Finally, tetravalent dopants (M = Ge, Ti, Sn, Zr and Ce) were considered on the Si site. Solution energy was calculated using the following reaction equation.

$$MO_2 + Si_{Si}^{X} \rightarrow M_{Si}^{X} + SiO_2 \qquad (19)$$

Table 9 reports the calculated solution energies. The promising dopant for this process is the Ge^{4+}. The preference of Ge^{4+} is due to the ionic radius of Si^{4+} (0.26 Å) is close to the ionic radius of Ge^{4+} (0.39 Å). Endoergic solution energy indicates that energy should be provided in the form of heat for this process. This is due to the stronger Si-O bonds present in the SiO_4 unit than Ge-O bonds present in GeO_4 unit. High solution enthalpies are observed for other dopants. In particular, solution enthalpies for TiO_2 and CeO_2 are approximately 3.50 eV, respectively, suggesting that they are highly unlikely to occur.

Formation of calcium vacancies was considered by doping of tetravalent dopants on the Al site as explained by the following equation.

$$2MO_2 + 2Al_{Al}^{X} + Ca_{Ca}^{X} \rightarrow 2M_{Al}^{\bullet} + V_{Ca}^{''} + Al_2O_3 \qquad (20)$$

Favorable dopant for this process is the Ge^{4+} (see Table 10). Finally, tetravalent dopants (M = Ge, Ti, Sn, Zr and Ce) were considered on the Si site. Solution energy was calculated using the following reaction equation.

Formation of Ca vacancies is favored by the doping of Ge^{4+} though this process is endoergic with the solution energy of 2.50 eV. High solution energies (>3.50 eV) are calculated for other dopants meaning that they are highly unfavorable.

3.5. Ca-diffusion in the presence of dopants

\Here we calculate the activation energies for Ca-ion diffusion in the presence of most favorable dopants (Sr^{2+} on the Ca site, Fe^{3+} on the Al site and Ge^{4+} on the Si site). Table 11 shows the activation energies for the local Ca hops and the long-range diffusion pathways. There is a very small reduction (by ~0.10 eV) in the activation energies can be due to the ionic radius mismatch between host and guest ions. The current simulation considered the doping at dilute limit. Once the doping concentration increases the further reduction in the activation can be expected.

4. Conclusions

In this study, atomistic simulation techniques are used to understand the defect energetics, diffusion of Ca-ion and solution of dopants. The Al–Si anti-site is found to be the most dominant defect inferring the cation disorder in this material as observed in the experiment. The second most favorable defect is the O-Frenkel. The Ca-ion diffusion pathway takes place in the ac plane exhibiting low ionic conductivity. The candidate isovalent dopants on the Ca, Al and Si sites are Sr, Fe and Ge respectively. Additional Ca or oxygen vacancies can be introduced by doping Fe^{3+} on the Si site. The formation of calcium vacancies is favored by doping of Ge on the Al site. The present study aims to simulate further experimental work on the doped $CaAl_2Si_2O_8$.

Acknowledgments

Imperial College London, Coventry University and the University of Jaffna are acknowledged for providing high-performance computing facilities.

Disclosure statement

No potential conflict of interest was reported by the authors.

ORCID

Navaratnarajah Kuganathan http://orcid.org/0000-0002-4826-5329

References

[1] King R. Minerals explained 23: Plagioclase feldspars. Geol. Today. 1997;13:117–20.
[2] Nawaratne SW. Feldspar and vein quartz mineralization in Srilanka: a possible post metamorphic mid-paleozoic pegmatitic-pneumatolitic activity. J Geol Soc Srilanka. 2009;13:83–96.
[3] Nawaratne SW, Liyanage ULNI. Industrial applications of the minerals in the matale area and its future trends. Ceylon J Sci. 2014;18:17–26.
[4] Taylor M, Brown GE. Structure of mineral glasses—I. The feldspar glasses $NaAlSi_3O_8$, $KAlSi_3O_8$, $CaAl_2Si_2O_8$. Geochim Cosmochim Acta. 1979;43:61–75.
[5] Agathopoulos S, Tulyaganov DU, Marques PAAP, et al. The fluorapatite–anorthite system in biomedicine. Biomaterials. 2003;24:1317–1331.
[6] Kavalci S, Yalamaç E, Akkurt S. Effects of boron addition and intensive grinding on synthesis of anorthite ceramics. Ceram Int. 2008;34:1629–1635.
[7] Kurama S, Ozel E. The influence of different CaO source in the production of anorthite ceramics. Ceram Int. 2009;35:827–830.
[8] Ke S, Cheng X, Wang Y, et al. Dolomite, wollastonite and calcite as different CaO sources in anorthite-based porcelain. Ceram Int. 2013;39:4953–4960.
[9] Arroyo-de Dompablo ME, Ponrouch A, Johansson P, et al. Achievements, challenges, and prospects of calcium batteries. Chem Rev. 2020;120:6331–6357.
[10] Torres A, Luque FJ, Tortajada J, et al. Analysis of minerals as electrode materials for Ca-based rechargeable batteries. Sci Rep. 2019;9:9644.
[11] Kuganathan N, Ganeshalingam S, Chroneos A. Defect, transport, and dopant properties of andradite garnet $Ca_3Fe_2Si_3O_{12}$. AIP Adv. 2020;10:075004.
[12] Kuganathan N, Chroneos A. Defects and Dopants in CaFeSi2O6: Classical and DFT Simulations. Energies. 2020;13:1285.
[13] Pal M, Das S, Das SK. Anorthite porcelain: synthesis, phase and microstructural evolution. Bull Mater Sci. 2015;38:551–555.
[14] Harabi A, Zaiou S, Guechi A, et al. Mechanical properties of anorthite based ceramics prepared from kaolin DD2 and calcite. Cerâmica. 2017;63:311–317.
[15] Yasmin Y, Mazlee MN, Norzilah AH, et al. The investigation of physical and mechanical properties of porous anorthite ceramics using statistical analysis. AIP Conf Proc. 2016;1756:090011.
[16] Le Parc R, Champagnon B, Dianoux J, et al. $CaAl_2Si_2O_8$ glass: low frequency Raman spectroscopy and neutron scattering. J Non-Cryst Solids. 2003;323:155–161.
[17] Angel RJ. Order-disorder and the high-pressure P1-I1 transition in anorthite. Am Mineral. 1992;77:923–929.
[18] Aliyu ZS, Garkida AD, Ali EA, et al. Characterization of Feldspar by instrumental analytical techniques. in: characterization of minerals, metals, and materials 2015. Carpenter JS, Bai C, Escobedo JP, et al., editors. Cham: Springer International Publishing; 2016. p. 291–297.
[19] Chevrel MO, Giordano D, Potuzak M, et al. Physical properties of $CaAl_2Si_2O_8$–$CaMgSi_2O_6$–FeO–Fe_2O_3

melts: analogues for extra-terrestrial basalt. Chem Geol. 2013;346:93–105.
[20] McGuinn MD, Redfern SAT. Ferroelastic phase transition along the join $CaAl_2Si_2O_8$-$SrAl_2Si_2O_8$. Am Mineral. 1994;79:24–30.
[21] Karki BB, Bohara B, Stixrude L. First-principles study of diffusion and viscosity of anorthite ($CaAl_2Si_2O_8$) liquid at high pressure. Am Mineralo. 2011;96(5–6):744–751.
[22] Noritake F, Kawamura K, Matsukage KN. Matsukage KN. Elastic anomalies of anorthite: molecular dynamics simulations. Phys Earth Planet Inter. 2015;244: 32–41.
[23] Zhang F, Liu X, He X, et al. A periodic density functional theory study of adsorption of CO_2 on anorthite (001) surface and effect of water. J Theoretical Computational Chemi. 2019;18(2):1950010.
[24] Kuganathan N, Srikaran R, Fossati CMP, et al. Theoretical modeling of defects, dopants, and diffusion in the mineral ilmenite. Minerals. 2019;9:610.
[25] Kuganathan N, Iyngaran P, Vovk R, et al. Defects, dopants and Mg diffusion in $MgTiO_3$. Sci Rep. 2019;9:4394.
[26] Islam MS, Fisher CAJ. Lithium and sodium battery cathode materials: computational insights into voltage, diffusion and nanostructural properties. Chem Soc Rev. 2014;43:185–204.
[27] Freeman CM, Catlow CRA. A computer modeling study of defect and dopant states in SnO_2. J Solid State Chem. 1990;85:65–75.
[28] Battle PD, Bush TS, Catlow CRA. Structures of quaternary Ru and Sb oxides by computer simulation. J Am Chem Soc. 1995;117:6292–6296.
[29] Gale JD, Rohl AL. The General Utility Lattice Program (GULP). Mol Simul. 2003;29:291–341.
[30] Lewis GV, Catlow CRA. Potential models for ionic oxides. J Phys C Solid State Phys. 1985;18:1149.
[31] Fisher CAJ, Kuganathan N, Islam MS. Defect chemistry and lithium-ion migration in polymorphs of the cathode material Li_2MnSiO_4. J Mater Chem A. 2013;1:4207–4214.
[32] Gale JD. GULP: a computer program for the symmetry-adapted simulation of solids. J Chemi Soci Faraday Transact. 2014;43(4):185–204.
[33] Mott NF, Littleton MJ. Conduction in polar crystals I. Electrolytic conduction in solid salts. Trans. Faraday Soc. 1938;34:485–499.
[34] Kuganathan N, Ganeshalingam S, Chroneos A. Defects, diffusion, and dopants in $Li_2Ti_6O_{13}$: atomistic simulation study. Materials. 2019;12:2851.
[35] Grimes RW, Busker G, McCoy MA, et al. The effect of ion size on solution mechanism and defect cluster geometry. Ber Bunsen Phys Chem. 1997;101: 1204–1210.
[36] Bruno E, Chiari G, Facchinelli A. Anorthite quenched from 1530°C. I. Structure refinement. Acta Crystallogr. B. 1976;32: 3270–3280.
[37] Kröger FA, Vink HJ. Relations between the Concentrations of Imperfections in Crystalline Solids. In: Solid State Physics, Seitz F, Turnbull D. (Eds.), 956;3:307–435. New York: Academic Press.
[38] Armstrong AR, Kuganathan N, Islam MS, et al. Structure and lithium transport pathways in Li_2FeSiO_4 cathodes for lithium batteries. J Am Chem Soc. 2011;133:13031–13035.
[39] Kempaiah Devaraju M, Duc Truong Q, Hyodo H, et al. Synthesis, characterization and observation of antisite defects in $LiNiPO_4$ nanomaterials. Sci Reports. 1985;18 (1):11041.
[40] Kuganathan N, Gkanas EI, Chroneos A. Mg_6MnO_8 as a magnesium-ion battery material: defects, dopants and Mg-Ion transport. Energies. 2019;12:3213.
[41] Politaev VV, Petrenko AA, Nalbandyan VB, et al. Crystal structure, phase relations and electrochemical properties of monoclinic Li_2MnSiO_4. J Sol State Chemi. 2011;133(3):13031–13035.
[42] Dompablo MEA, De Krich C, Nava-Avendaño J, et al. Joint computational and experimental evaluation of $CaMn_2O_4$ polymorphs as cathode materials for Ca ion batteries. Chem Mater. 2016;28:6886–6893.
[43] Islam MS, Driscoll DJ, Fisher CAJ, et al. Atomic-scale investigation of defects, dopants, and lithium transport in the $LiFePO_4$ olivine-type battery material. Chem Mater. 2005;17:5085–5092.
[44] Nishimura S-I, Kobayashi G, Ohoyama K, et al. Experimental visualization of lithium diffusion in $Li_x FePO_4$. Nat Mat. 2019;12(9):707.